Icarus 280 (2016) 183–198

Contents lists available at ScienceDirect

Icarus

journal homepage: www.elsevier.com/locate/icarus

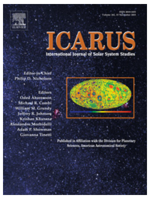

Lunar iron and optical maturity mapping: Results from partial least squares modeling of Chang'E-1 IIM data

Lingzhi Sun[a], Zongcheng Ling[a,b,*], Jiang Zhang[a], Bo Li[a], Jian Chen[a], Zhongchen Wu[a], Jianzhong Liu[c]

[a] Shandong Provincial Key Laboratory of Optical Astronomy & Solar-Terrestrial Environment, Institute of Space Sciences, Shandong University, Weihai 264209, China
[b] Key Laboratory of Lunar and Deep Space Exploration, Chinese Academy of Sciences, Beijing 100012, China
[c] Institute of Geochemistry, Chinese Academy of Sciences, Guiyang 550002, China

ARTICLE INFO

Article history:
Received 4 March 2016
Revised 4 July 2016
Accepted 20 July 2016
Available online 27 July 2016

Keywords:
Moon, surface
Spectroscopy
Mineralogy

ABSTRACT

Iron and optical maturity (OMAT) are two key geological marks of the Moon that closely related to its geochemical evolution and interactions between surface and space environment. We apply Partial Least Squares (PLS) regression to Chang'E-1 Imaging Interferometer (IIM) (32 bands between 480 and 960 nm) in mapping lunar global FeO and OMAT, and the FeO and OMAT values are derived based on reasonable spectral parameters (absorbance, band ratios, TiO_2 and maturity sensitive parameters, etc.). After been calibrated by the FeO map from Lunar Prospector Gamma-Ray Spectrometer (LP-GRS), the global FeO map derived from PLS modeling shows a quantitatively more reasonable result consistent with previous remote sensing results (LP) as well as lunar feldspathic meteorite studies and Chang'E-3 landing site. Based on the new FeO map by Chang'E-1, we discover a compositional inhomogeneity across lunar highland regions, which has not been suggested by previous datasets (e.g., Clementine UVVIS). Furthermore, we suggest that at least part of the FeO enrichments in highlands would be caused by mixing of highland and mare materials. The IIM derived OMAT map does not suggest a dichotomy of the lunar highlands and mare regions, implying the compositional differences between those two terrains have been suppressed. We further check the maturity effect for the young mare basalts (<3.0 Ga), and find that (1) the OMAT values of the young basaltic units with medium and high FeO and TiO_2 show a linear decrease with ages; (2) units with ultrahigh-FeO (>20 wt%) and ultrahigh-TiO_2 (>10 wt%) tend to have greater OMAT values and vary little with ages; (3) this may be due to the distinct optical maturity effects of ultramafic minerals (i.e., ultrahigh Fe and Ti) and/or the spectral blue shifts of abundant ilmenite.

1. Introduction

Iron is one of the most abundant and varying rock-forming elements on the Moon, whose accurate quantification and global distribution are important for the recognition of mineralogy and crustal evolution (Lucey et al., 2000a; Lucey et al., 1995). In comparison with the analysis of the limited number of samples from known (e.g., Apollo and Luna samples) or unknown (e.g., lunar meteorites) locations, lunar remote sensing studies can obtain datasets at high spectral (e.g., Moon Mineralogy Mapper, ~10 nm, Green et al., 2011) and spatial resolutions (e.g., Multiband Imager, ~20 m, Ohtake et al., 2008), and thus provide a fine scale and comprehensive global view of the Moon. As the Moon has been exposed to the space environment for billions of years since its formation, impactors like meteorites and solar wind particles have been working on the lunar surface materials and generating space weathering products in the lunar soils, including the reduction of soil particle size, the accumulation of submicroscopic metallic Fe (SMFe) and the production of agglutinates (Fischer and Pieters, 1994; Hapke, 2001; Pieters et al., 2000; Wilcox et al., 2005). Space weathering products darken and redden the ultraviolet, visible and near-infrared (UV–vis–NIR) spectra and attenuate absorption depth (typically located at 1 µm and/or 2 µm from Fe^{2+} in mafic minerals) (Fischer and Pieters, 1996). The degree of space weathering can be described by the term "maturity", and higher degree of maturity represents a longer time of exposure to the space (Lucey et al., 2000b; McKay et al., 1991; Wilcox et al., 2005). Space weathering effect is common for airless bodies in Solar System and need

---

* Corresponding author at: Shandong Provincial Key Laboratory of Optical Astronomy and Solar-Terrestrial Environment, Institute of Space Sciences, Shandong University, Weihai 264209, China.
E-mail address: zcling@sdu.edu.cn (Z. Ling).

http://dx.doi.org/10.1016/j.icarus.2016.07.010
0019-1035/

to be decoupled when mapping elemental information from the remotely acquired VIS–NIR spectral data.

There have been many attempts using VIS reflectance and NIR/VIS ratio (e.g., 750 nm and 950/750 nm for Clementine UVVIS as well as Multiband Imager datasets) and Clementine NIR data to derive the abundance of FeO with efforts to suppress the maturity effects from lunar soils spectra (Blewett et al., 1997; Fischer and Pieters, 1994; Fischer and Pieters, 1996; Gillis-Davis et al., 2006; Gillis et al., 2004; Le Mouélic et al., 2000; Le Mouélic et al., 2002; Lemelin et al., 2015; Lucey et al., 2000a; Wilcox et al., 2005). In addition to the above empirical band-ratio methods, statistical regression method such as Multiple Linear Regression (MLR), Principle Component Analysis (PCA), and Partial Least Squares Regression (PLS) are also widely used in the derivation of lunar chemical abundances from remotely-sensed as well as laboratory measured spectral datasets (e.g., Li, 2006, 2008; Pieters et al., 2006; Pieters et al., 2002; Shkuratov et al., 2003). Pieters et al. (2002) studied the relations among lunar mare mineralogy and chemistry and reflectance data from Lunar Soil Characterization Consortium (LSCC) by PCA, and then built a series of statistical equations for the estimation of mineral abundances. They then derived the global distribution of pyroxene minerals content and maturity parameters using the Clementine UVVIS dataset (Pieters et al., 2006). PLS is effective in resolving the mutual influence of variables and has been widely applied in chemical and mineral estimations of Moon and Mars (e.g., Cousin et al., 2015; Cousin et al., 2012; Dyar et al., 2012; Li, 2006, 2008). Li (2006) quantified the abundance of lunar soil chemical compositions (including FeO and TiO_2) with LSCC spectral reflectance data using PLS and PCA regression, and PLS is preferred to PCA for using fewer components during regression. Later, Li (2008) transformed the spectral data of LSCC into single scattering albedo to evaluate the ability of PLS and PCA for estimating the abundance of FeO, Al_2O_3 and TiO_2. Cousin et al. (2015) used PLS to retrieve elemental compositions from the Laser Induced Break-down Spectroscopy (LIBS) spectra of Martian soils derived by the ChemCam onboard the Curiosity rover.

Many efforts have estimated the abundance of FeO from the dataset of the first Chinese lunar hyperspectral imager, using both empirical band-ratio methods and statistical regression methods. i.e., Chang'E-1 IIM (Ling et al., 2016; Ling et al., 2011a; Wang et al., 2013; Wu, 2012; Wu et al., 2012; Yan et al., 2012). Using band-ratio method, Ling et al. (2011a) derived a FeO algorithm from IIM 757 nm and 891 nm/757 nm images, and produced a FeO map of southern Mare Crisium, which is consistent with Clementine results. Following similar methods but adopting the same hypermature endmember (i.e., x_{0Fe}=0.08, y_{0Fe}=1.19) as that of Clementine UVVIS data derived by Lucey et al. (2000a), Wu et al. (2012) derived the global distribution of iron and titanium using IIM data. Wu (2012) also applied PLS regression to derive the abundance of major elements (e.g., FeO, TiO_2, CaO, Al_2O_3, etc.) with IIM dataset, however, those models have been derived from the IIM spectral bands (22 bands from 561 to 918 nm) alone, which has limitations in maturity suppressing. Wang et al. (2013) claimed that 891 nm performs better than 918 nm for its higher accuracy in FeO derivation with IIM data. Yan et al. (2012) made a global FeO map using IIM data and lunar sampling stations published by Lucey et al. (2000a), and the global FeO content ranges from 0 to 21 wt% based on their study. However, most of the former IIM FeO models did not take the influence of TiO_2 content into account or ignored the space weathering effect. Here we report our work on FeO and OMAT mapping using the PLS method. The goal of this work is to explore the utility of IIM hyperspectral data for FeO and OMAT mapping, and to compare with previous remote sensing derived estimates (e.g. Clementine UVVIS and Lunar Prospector). Different combinations of spectral parameters (reflectance, band ratios, TiO_2 and maturity sensitive parameters) will be tested and compared in order to derive a robust PLS-derived FeO and OMAT models with Chang'E-1 IIM dataset.

2. Data descriptions

2.1. IIM data set and lunar sampling stations

Chang'E-1 IIM is the first Sagnac-based push-broom imaging spectrometer to collect data of the Moon, with the goal to collect the compositional and mineralogical properties of lunar surface materials. With a global coverage of ~78% at 200 m/pixel spatial resolution (Ling et al., 2011b), data from IIM have higher spectral sampling from 480 to 960 nm than provided by other instruments, and therefore has great potential for improved compositional and space weathering mapping. While due to the limited response of the CCD detector, we only use bands from 513 to 891 nm, which have good signal to noise ratios (Ling, 2011; Ling et al., 2011a, Supplementary Table S1). The IIM level 2A dataset used in this work has been processed with dark current and flat-field calibration, radiometric calibration, etc. (Ling et al., 2011a) and released by Ground Research and Application System (GRAS) of Chang'E-1 Project (Zuo et al., 2014). In addition, the data we used has undergone photometric calibration (Zhang et al., 2013), and empirical flat-filed corrections and spectral calibrations (Ling et al., 2012, 2014b), in order to further remove residual artifacts of IIM datasets.

PLS modeling requires chemical compositions associated with spectra to quantify the statistical relationship between spectral and compositional properties. We use IIM spectra of Apollo and Luna landing sites for which chemical analysis is available from measurement of soils from those locations from the Moon (Table 1 and supplementary Table S2). The chemical compositions of representative samples from Apollo and Luna sampling sites are ground truths for lunar remote sensing studies. Therefore, the accurate positioning of these sites is very important for the FeO and OMAT mapping using Chang'E-1 IIM dataset. We carefully located the 38 sampling sites within IIM images by visual inspection with the aid of the high spatial resolution images from Lunar Reconnaissance Orbiter Camera (LROC) (Robinson et al., 2010), where most of the sampling site can be discerned in detail by recognizing their surrounding geological features (see supplementary material Fig. S1). Finally, all the Apollo and Luna sampling stations except Apollo 15 are resolved in IIM images (Table 1). The typical spectra of the stations are averaged by 2 × 2 or 3 × 3 pixels in order to improve their signal-to-noise ratios.

The abundances of FeO used as the inputs of PLS model are from compositions of sampling-site soils (Blewett et al., 1997; Lucey et al., 2000a). OMAT values for the modeling inputs are calculated by the equations from Lucey et al. (2000b) using Clementine UVVIS data (from Table 2 of Wilcox et al., 2005). The range of the FeO content for the sampling sites listed in Table 1 is about 4–20 wt%. Most of the low-Fe data points come from Apollo 16 lunar soils, which are known not to be typical lunar highland samples (Gross et al. 2014; Warren, 1990). Thus we add a spectrum from the wall of South Ray crater, which may consist of pure anorthosite (PAN) (Ohtake et al., 2009). The FeO content of this site is regarded as 0.5 wt% (Adams and Goullaud, 1978), and TiO_2 content (0.032 wt%) is calculated based on equations from Ling, Zhang, and Liu (2013), and OMAT value is 0.3, which was calculated from the same location of Clementine images by equations from Lucey et al. (2000b). Fresh lunar regions typically have OMAT values exceeding 0.25 (Lucey et al., 2014), while the OMAT values of most sampling sites included are less than 0.2, except the Apollo 16-S11 site. Thus

Table 1
Lunar sampling stations' coordinates in LROC images, composition and optical maturity (OMAT).

Site	Orbit no.	Latitude,°N	Longitude, °E	boxes	FeO (wt%)	TiO_2 (wt%)	OMAT
Apollo 11	2218	0.6733	23.4847	3×3	15.8	7.5	0.13
Apollo 12	2567	−3.0089	−23.4179	3×3	15.4	3.1	0.17
Apollo 14-LM	2562	−3.6453	−17.4714	2×2	10.5	1.73	0.14
Apollo 14-Cone	2562	−3.6327	−17.4714	2×2	10.3	1.6	0.15
Apollo 16-LM	2224	−8.9731	15.5002	2×2	5.6	0.6	0.16
Apollo 16-S1	2224	−8.9767	15.4481	2×2	5.4	0.6	0.17
Apollo 16-S2	2224	−8.9734	15.4762	2×2	5.5	0.6	0.18
Apollo 16-S4	2224	−9.0997	15.5180	2×2	4.6	0.5	0.17
Apollo 16-S5	2224	−9.0811	15.5170	2×2	5.9	0.7	0.16
Apollo 16-S6	2224	−9.0687	15.5051	2×2	6	0.7	0.18
Apollo 16-S8	2224	−9.0643	15.4814	2×2	5.4	0.6	0.19
Apollo 16-S9	2224	−9.0543	15.4868	2×2	5.7	0.6	0.17
Apollo 16-S11	2224	−8.8298	15.4970	2×2	4.2	0.4	0.23
Apollo 16-S13	2224	−8.8502	15.5114	2×2	4.8	0.5	0.20
Apollo 17-LM	2212	20.1908	30.7717	2×2	16.6	8.5	0.14
Apollo 17-S1	2212	20.1598	30.7814	2×2	17.8	9.6	0.17
Apollo 17-S2	2212	20.1028	30.5326	2×2	8.7	1.5	0.16
Apollo 17-S3	2212	20.1739	30.5657	2×2	8.7	1.8	0.15
Apollo 17-S5	2212	20.1862	30.7249	2×2	17.7	9.9	0.14
Apollo 17-S6	2212	20.2897	30.7939	2×2	10.7	3.4	0.13
Apollo 17-S7	2212	20.2898	30.8091	2×2	11.6	3.9	0.14
Apollo 17-S8	2212	20.2772	30.8683	2×2	12.3	4.3	0.13
Apollo 17-S9	2212	20.2338	30.8265	2×2	15.4	6.4	0.14
Apollo 17-LRV1	2212	20.1775	30.6849	2×2	16.3	8	0.14
Apollo 17-LRV2	2212	20.1834	30.6435	2×2	13.4	4.4	0.13
Apollo 17-LRV3	2212	20.1857	30.6297	2×2	14.8	5.5	0.12
Apollo 17-LRV4	2212	20.1146	30.5490	2×2	8.5	1.3	0.15
Apollo 17-LRV5	2212	20.1874	30.5897	2×2	9.8	2.6	0.15
Apollo 17-LRV6	2212	20.1990	30.5976	2×2	10.3	2.6	0.14
Apollo 17-LRV7	2212	20.2175	30.6672	2×2	16.1	6.8	0.12
Apollo 17-LRV8	2212	20.2072	30.6918	2×2	15.7	6.6	0.13
Apollo 17-LRV9	2212	20.2366	30.7771	2×2	14.6	6.1	0.12
Apollo 17-LRV10	2212	20.2806	30.7808	2×2	11.2	3.7	0.14
Apollo 17-LRV11	2212	20.2734	30.8619	2×2	12.7	4.5	0.14
Apollo 17-LRV12	2212	20.2004	30.8042	2×2	17.4	10	0.16
Luna 16	2189	−0.5129	56.3675	2×2	16.7	3.3	0.13
Luna 20	2189	3.7872	56.6216	2×2	7.5	0.5	0.13
Luna 24	2184	12.7148	62.2165	3×3	19.6	1	0.15
Apollo15-S9*[a]	2852	–	–	2×2	16.9	1.8	0.21
Pure Anorthosite[b]	2843	–	–	2×2	0.5	0.032	0.30

The compositions are from Table 1 from Lucey et al. (2000a), and the OMAT values are calculated with Eq. (1) from Lucey et al. (2000b) and Clementine reflectance spectra (Table 2 from Wilcox et al., 2005). The latitude and longitude of sampling sites are solved from LROC Quickmap by comparing to the LROC traverse maps.

[a] Apollo15-S9 is not covered by IIM data. This site is extracted from where the spectrum is the same with the original Apollo15-S9 site with Clementine UVVIS image (File Name: ui31n003).

[b] This site is a supplementary data for lunar highland regions located in the wall of South Ray crater, which is suggested to consist pure anorthosite by Ohtake et al. (2009).

Table 2
Coefficients (C refers to *p* in the OMAT model and a, b, c in FeO-1–FeO-3) of the PLS models.

models	C0	C1	C2	C3	C4	C5	C6	C7
OMAT	−0.495	−0.131	0.0089	−0.491	0.632	1.089	−0.498	−0.0012
FeO-1	−10.097	11.271	−11.854	−26.334	40.448	20.011	40.04	−62.693
FeO-2	−15.575	−3.069	−2.985	−3.479	23.35	0.037	16.803	–
FeO-3	−14.747	1.377	−4.981	−4.269	22.127	−2.691	18.222	–

we add the additional fresh data point of Apollo 15-S9*, which can also be served as supplementary data of low-Ti, High-Fe soil (Ling et al., 2011a). As all the Apollo 15 sampling sites are not covered by IIM images, we tend to find a substitute site (Apollo 15-S9*) that has the same spectrum with Apollo 15-S9 using Clementine UVVIS digital image model from U.S. Geological Survey (USGS). Apollo 15-S9* is located by spectral matching (least root-mean-squares error) of Apollo 15-S9 sampling station with its surrounding Clementine UVVIS images (File Names: ui24n003.img, ui31n003.img), and the optimum location is found in Clementine file ui31n003.img. The corresponding Apollo 15-S9* site for IIM data is then located by connecting IIM image (Orbit Number: 2852) with Clementine image (File Name: ui31n003.img) using ground control points (GCPs).

2.2. Data processing and partial least squares regression

The PLS models are built using PLS_toolbox from Eigenvector Research, Inc. (http://www.eigenvector.com/software/pls_toolbox.htm). PLS has been proved to be effective to derive lunar soils chemical compositions from VIS–NIR spectral data (e.g., Li, 2006) as well as terrestrial soil contamination (e.g., Kooistra et al., 2001). As an advanced multivariate statistical method, PLS is aimed to find the best latent variables (LVs) based on maximum covariance between variables. PLS as a statistical method can be considered as a combination of principle component analysis (PCA) and classical component analysis (CCA). Supposing the matrix of predictor is X (Dimensions $= n \times m$), which is measured from n sampling stations and m variables (e.g., spectral bands, ratios), and the matrix of response is Y (Dimensions $= n \times p$), which is measured from n sampling stations and p variables (e.g., FeO content or OMAT value, $p = 1$ in this study). X and Y can be decomposed into the right side of Eqs. (1) and (2). T and U are the score matrixes of X and Y, and their dimensions are $n \times a$; P and Q are loading matrixes of X and Y, and their dimensions are $m \times a$ (a is the number of latent variables). E and F are the error matrixes, and their dimensions are same to X and Y respectively. The rule of the decomposition shown in Eqs. (1) and (2) is to maximize the covariance between T and U, and then the correlation relation between T and U can be derived (Eq. (3)), B is the regression coefficient matrix ($n \times n$). Bring Eqs. (1) and (3) into Eq. (2), we can get Eq. (4), which is the correlation relation between X and Y.

$$X = TP^T + E \tag{1}$$

$$Y = UQ^T + F \tag{2}$$

$$U = BT \tag{3}$$

$$Y = XB + F \tag{4}$$

Before modeling, all the reflectance spectra are transformed into absorbance by applying a natural logarithmic function (Eq. (5), R refers to reflectance and A refers to absorbance, Li, 2006). This relation can be derived based on Beer's Law assuming zero transmittance and small A. Absorbance is assumed to correlate linearly with the abundance of chemicals (Li, 2006; Yen et al., 1998). Owing to the limited number of sampling stations that extracted from IIM images, all the data are used as the modeling set. In order to get a more robust result, all the data are mean centered (i.e., subtracting the mean value from the original data) before modeling. Leave-one-out cross validation (CV) is executed during the modeling to find the best LV number (Li, 2006). Among data from 40 stations, 39 of them is used to build the PLS model, and 1 sampling site is left out as validation data. Repeating this process until each data has been left out once and we can get the root-mean-square error for all the CV models (RMSECV, Eq. (6)) (Li, 2006). During the modeling, the LV number is corresponding to the CV model with minimum RMSECV.

$$-\ln(R) = -ln(1 - A) \approx A \tag{5}$$

$$\text{RMSECV} = \sqrt{\frac{\sum_{i=1}^{40} (\hat{y}_i - y_i)^2}{40}} \tag{6}$$

3. Correlations between IIM data and chemicals

We examine the correlations between chemical abundances (i.e., FeO, TiO_2), OMAT and IIM spectral bands for 40 lunar sites at first, with intent to find the most optimum spectral parameters (i.e., spectral bands and ratios) for the PLS modeling. The univariate correlations between the absorbance of IIM spectral bands and the abundance of FeO, TiO_2 and OMAT values are shown in Fig. 1a, and these correlation coefficients vary very little with IIM spectral bands. The band ratios of IIM spectral data from 40 lunar locations are correlated with FeO, TiO_2 and OMAT respectively, as shown in Fig. 1b, c and d. Each point in these three figures represents the correlation coefficient between the ratio of the related bands (corresponding band in y axis versus band in x axis) and the abundances of FeO or TiO_2 or OMAT values. Here we will discuss these correlation relationships in detail.

FeO: FeO is highly correlated with absorbance over all IIM bands, and the correlation coefficients do not vary substantially (higher than 0.95, and the maximum value is 0.966). In contrast, for band ratios, high correlations seem to concentrate in the upper left and lower right triangle in Fig. 1b, which indicates that larger interval of two bands may yield a better estimation of FeO for the spectral ratio. The three ratios with largest correlation coefficients are 841 nm/531 nm (0.88), 891 nm/531 nm (0.877), 865 nm/531 nm (0.871). While the band ratio 891 nm/757 nm used by Ling et al. (2011, 2013) in the derivation of FeO only has a coefficient of about 0.48 based on our modeling.

OMAT: OMAT correlates inversely with absorbance (Fig. 1a). Most of the coefficients for IIM bands are around −0.65, and the best is −0.666 (513 nm). For band ratios, the highest correlation is 541 nm/797 nm (0.765), and the other two high correlations are 541 nm/673 nm (0.755), 541 nm/704 nm (0.751).

TiO_2: Absorbance over all IIM bands are highly correlated with TiO_2 abundance with an average correlation of ~0.81, and the highest correlations occur at band 738 nm (0.824), 688 nm (0.82), 757 nm (0.817) and 721 nm (0.817).The highest correlation coefficient between TiO_2 abundance and IIM band ratios is about 0.8 (738 nm/631 nm), and the correlations higher than 0.75 are located at 738 nm/531 nm (0.8), 757 nm/531 nm (0.768) and 738 nm/513 nm (0.758), respectively. This correlation result is consistent with the band ratio 757 nm/522 nm (0.716) used by Ling et al. (2011, 2013) in the TiO_2 derivation.

4. Partial least squares modeling

4.1. Estimating the degree of optical maturity

Optical maturity (OMAT) is a parameter to measure the space weathering effect by lunar remote sensing (Lucey et al., 2000b). OMAT values using Clementine UVVIS data is defined as the Euclidean distance of a point to the theoretical hyper-mature origin in a 950/750 nm versus 750 nm plot (Lucey et al., 2000b). Although OMAT can be derived based on a similar algorithm from IIM spectra (e.g., Ling et al., 2013), our goal is to build a robust OMAT model with multiple spectral parameters, and test its ability in suppressing the uncertainties caused by chemical compositions (i.e., FeO, TiO_2) by comparing to Clementine OMAT values (Lucey et al., 2000b).

The degree of lunar surface optical maturity is first estimated using PLS modeling, and the modeling data is given in Table 1 and supplementary Table S2. As discussed in Section 3, maturity is correlated with spectral ratios, thus band ratios can be used to reproduce maturity parameters. Three band ratios best correlated with OMAT (541 nm/797 nm, 541 nm/673 nm, 541 nm/704 nm) and four spectral bands are included as modeling parameters. Since the correlation coefficients of all the spectral bands are similar to each other, we apply a cycle modeling method to find the most optimum combination of spectral bands: firstly, four bands (e.g., bands 1–4) are chosen from 26 available bands, and we combine these four bands with the three band ratios above to build a PLS model; secondly, we apply this model to the test region on southern rim of Mare Crisium (Fig. 4a, center coordinate: 61°E, 11°N) to evaluate its ability in the derivation of OMAT. These band selection processes were repeated 14,950 times until all the combinations of the 4 bands out of 26 bands have been modeled and applied to the test region once. Finally, the best spectral bands are determined based on both the regression coefficients of the PLS regression and the standard deviation of the OMAT map of the test region. A higher regression coefficient indicates a better PLS regression and a lower standard deviation indicates a better ability in suppressing the compositional differences of OMAT values between highland and mare regions. Base on the above rules, we derive the most optimum spectral parameters for the OMAT model as shown in Eq. (7). In Eq. (7), A represents absorbance, and the subscript

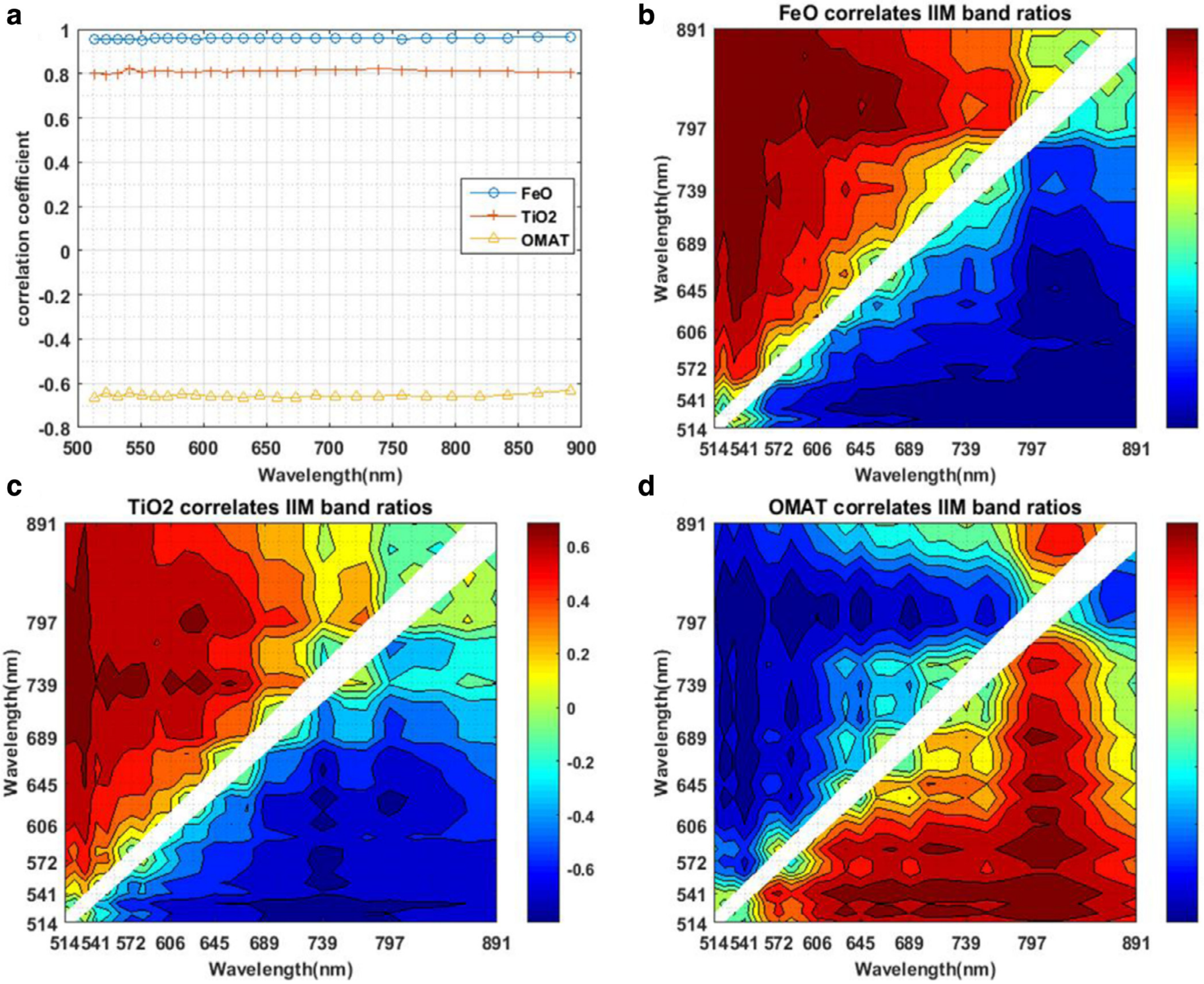

Fig. 1. Correlations of IIM modeling data and chemical abundances. (a) Correlations between spectral bands and FeO, TiO_2, and OMAT respectively, (b) correlation between FeO and band ratios, the ratio of each point refers to the band on *y* axis versus band on *x* axis (c) correlation between OMAT and band ratios, (d) correlation between TiO_2 and band ratios.

refers to wavelength of the IIM spectral channels in nanometer, p_0 – p_7 are regression coefficients (Table 2). In this case, the four absorption bands and three ratios refers to *X* and OMAT refers to *Y* during the PLS modeling.

$$\mathrm{OMAT} = p_0 + p_1 A_{541} + p_2 A_{618} + p_3 A_{704} + p_4 A_{891} + p_5 \frac{A_{541}}{A_{797}} + p_6 \frac{A_{541}}{A_{673}} + p_7 \frac{A_{541}}{A_{704}} \quad (7)$$

The PLS regression result of the OMAT model is shown in Fig. 2a, where the points in the plot represent different sampling stations, and the coefficient of determination (R^2) is 0.878 and RMS is about 0.012. Considering the uncertainties of reflectance is less than 15% (Qiu et al., 2009; Zhang et al., 2013), we add a ±10% noise into the original IIM reflectance spectra of the sampling stations, and the corresponding error caused by this noise in the OMAT model is about ±2.6%. When applying the OMAT model (Eq. (7)) to IIM image (test region), we can derive the OMAT map (as shown in Fig. 3b). Comparing the derived IIM OMAT map with the Clementine UVVIS OMAT map of the same region calculated by Lucey et al. (2000b) algorithm (Fig. 3a), the former could also show the major variations of maturity. High OMAT values represent low maturity degree, and the red spots shown by Fig. 3a, b are fresh craters. From the histogram, our OMAT is consistent with the results of Lucey et al. (2000b), but IIM OMAT result is more uniformly distributed (Fig. 3c). The small peak pointed out by an arrow (Fig. 3c) in Lucey et al. (2000b) result, reveals a bimodal distribution of OMAT degree in lunar highland and mare regions. However, the small peak of highland materials is invisible in IIM result (Fig. 3c), indicating the IIM OMAT model is more efficient in suppressing lunar composition effects than that the band ratio algorithm.

4.2. PLS modeling for FeO

Here we conduct PLS regressions of FeO in terms of physical parameters, i.e., taking both the space weathering and compositional effects (TiO_2) into consideration. The modeling data are listed in Table 1 and supplementary Table S2. Spectral bands and band ratios are both adopted in the FeO model. The spectral

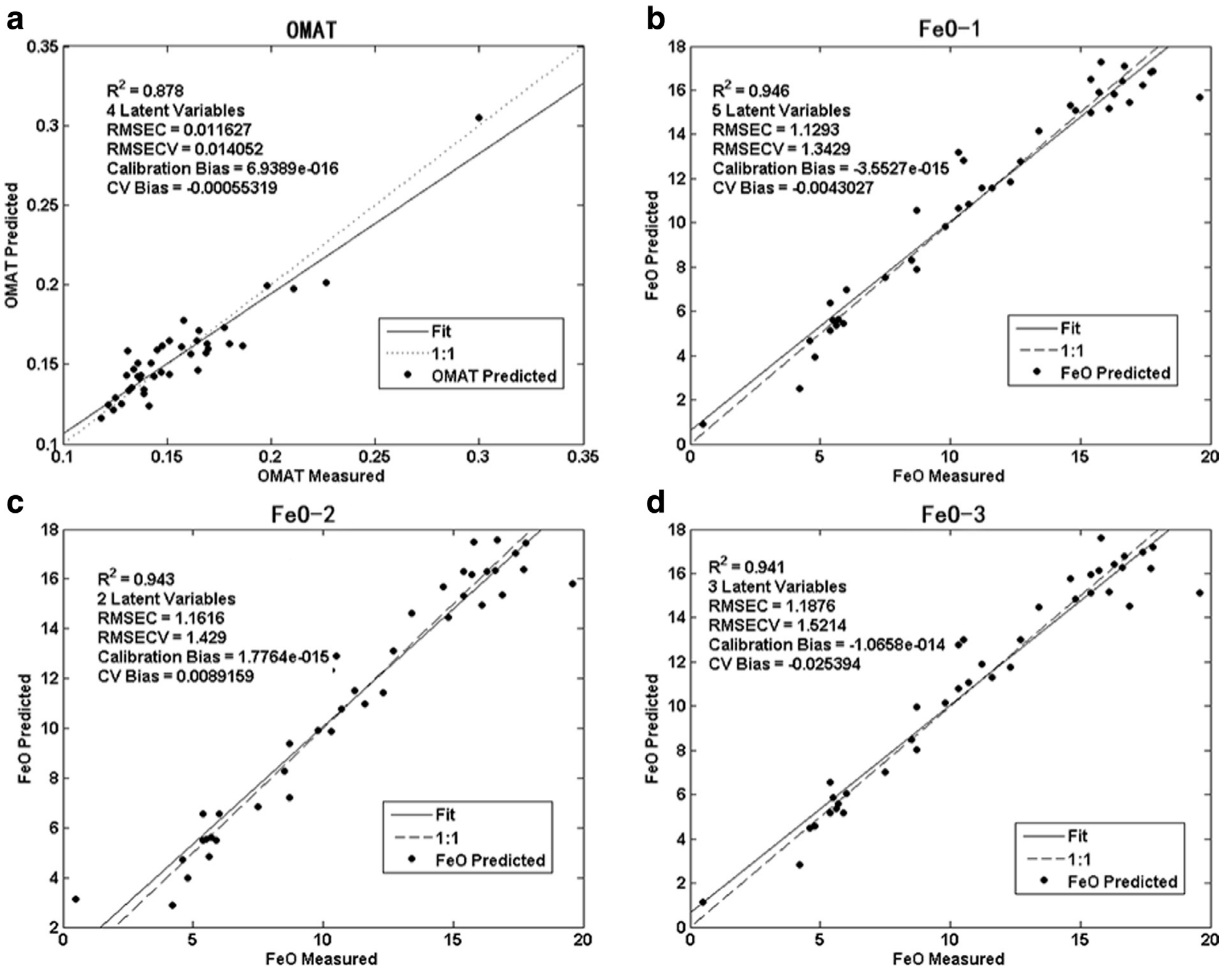

Fig. 2. Regression results of the PLS models. (a) The regression result of the OMAT model (Section 4.1). (b, c, and d) Regression results of the three FeO models resepctively (Section 4.2).

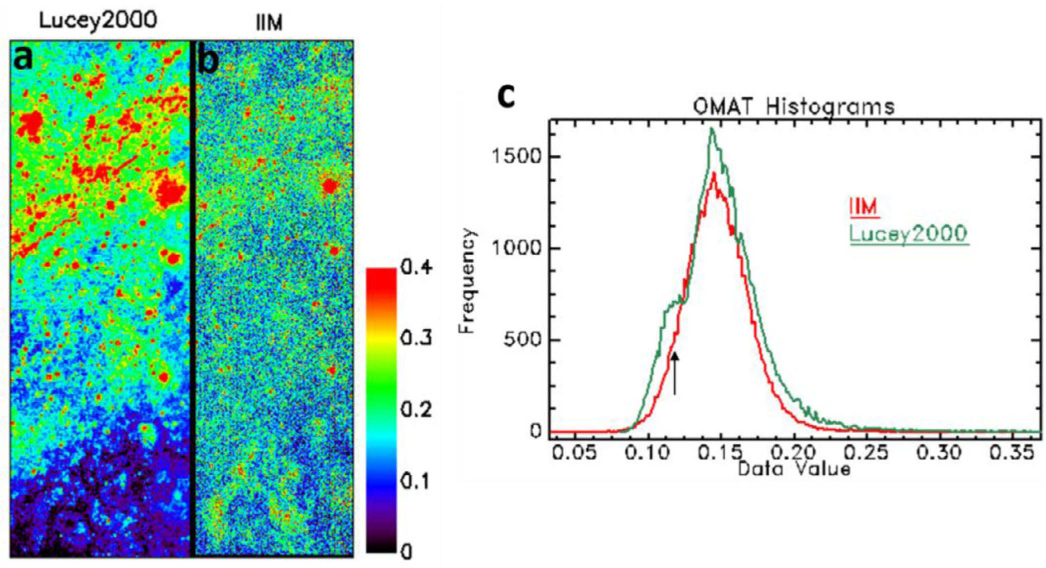

Fig. 3. Optical maturity (OMAT) maps of the test region (center coordinate: 61°E, 11°N). (a) Lucey et al. (2000b) result, (b) partial least squares (PLS) modeling result for IIM data using Eq. (7), high OMAT value refers to low maturity degree. (c) Histograms for (a) and (b).

ratios that best correlate with FeO, TiO_2 or OMAT are added into the FeO models for the suppression of compositional and/or maturity effects. The bands selection for FeO modeling follows the similar procedures to the OMAT modeling as discussed in Section 4.1. Three models (FeO-1–FeO-3, Eqs. (8)–(10)) using different parameters (bands, band ratios, OMAT and TiO_2 content) are examined in order to evaluate their ability in the derivation of FeO content while suppressing the maturity effect. In Eq. (8)–(10), A represents absorbance, and the subscript refers to wavelength of the IIM spectral channels in nanometer, a, b and c are regression coefficients (Table 2).

The first model (FeO-1, Eq. (8)) is built based on spectral parameters alone, which is widely used by former statistical studies in the derivation of chemical contents (Li, 2006, 2008; Pieters et al., 2006; Pieters et al., 2002; Shkuratov et al., 2003). We add three band ratios (891 nm/531, 865 nm/531 nm and 841 nm/531 nm) that best correlate with FeO abundances. Le Mouelic et al. (2000) suggested that band ratio could provide an evaluation of spectral alteration caused by space weathering effect. Besides, these ratios are well correlated with OMAT values, therefore, they can also contribute as maturity suppressing indexes. a_0–a_7 are PLS regression coefficients for the modeling (Table 2). In this case, the four absorption bands and 3 ratios refers to X and FeO refers to Y during the PLS modeling.

$$FeO-1 = a_0 + a_1A_{561} + a_2A_{594} + a_3A_{704} + a_4A_{891} + a_5\frac{A_{841}}{A_{531}} + a_6\frac{A_{865}}{A_{531}} + a_7\frac{A_{891}}{A_{531}} \tag{8}$$

Le Mouélic et al. (2000) and Gillis et al. (2004) pointed out that the abundance of TiO_2 would affect the abundance of the derived FeO. The presence of opaque minerals (dominated by TiO_2-rich ilmenite) will reduce the spectral contrast in iron-bearing silicates. To take the influence of titanium into consideration, two FeO models including parameters related to TiO_2 are built. TiO_2 abundances or OMAT values are directly added into the models to explore their ability in mineral or maturity suppressing, while at the same time, it is important to keep the independence of FeO model and avoid too much variances introduced from other algorithms. Therefore, we only add one extra term (TiO_2 abundance or OMAT value) into the next two FeO models (Eqs. (9) and (10)), and the other one is represented by spectral ratio that best correlate with TiO_2 abundance or OMAT value. In FeO-2 (Eq. (9)), band ratio 738 nm/631 nm is added as a TiO_2 sensitive parameter for its largest correlation coefficient, and OMAT performs as maturity sensitive parameter. b_0–b_6 are coefficients for Eq. (9) (Table 2). Model-3 (Eq. (10)) adds TiO_2 abundance to accommodate the variation of titanium content and the band ratio 541 nm/797 nm that best correlated with OMAT for the suppression of maturity. c_0–c_7 are coefficients for Eq. (10), as shown in Table 2.

$$\mathrm{FeO}-2 = b_0 + b_1A_{522} + b_2A_{594} + b_3A_{757} + b_4A_{865} + b_5\frac{A_{738}}{A_{631}} + b_6\mathrm{OMAT} \tag{9}$$

$$\mathrm{FeO}-3 = c_0 + c_1A_{561} + c_2A_{594} + c_3A_{704} + c_4A_{891} + c_5\mathrm{TiO_2} + c_6\frac{A_{541}}{A_{797}} \tag{10}$$

4.3. Regional validations of PLS-derived FeO

The PLS regression results of the FeO models are shown in Fig. 2, and the points in the plot represents FeO contents of the sampling stations. The coefficients of determination for all the three models are higher than 0.94. Considering the uncertainties of reflectance is less than 15% (Qiu et al., 2009; Zhang et al., 2013), we add a ±10% noise into the original IIM reflectance spectra of the sampling stations, and the corresponding error caused by this noise in the FeO models are: ±1.33 wt% (FeO-1), ±1.12 wt% (FeO-2) and ±2.20 wt% (FeO-3). As shown in Fig. 2, FeO-1 has the highest coefficient of determination ($R^2 = 0.946$) and lowest root-mean-square (RMS) value (1.129), and FeO-3 has the lowest coefficient of determination ($R^2 = 0.941$) and highest RMS value (1.188), FeO-2 provides an intermediate results ($R^2 = 0.943$, RMS = 1.162). However, the regression result should not be the only criteria for the evaluation of FeO modeling; further verification and validation is accomplished by applying these models to lunar spectral images. Two validation regions are selected for this purpose: one is from the south region of Mare Crisium (center coordinate: 61°E, 11°N, Fig. 4a), located around the border of mare and highland regions; the other one is from Oceanus Procellarum (center coordinate: 39.5°W, 15°N, Fig. 4b), and is suggested to be low-Ti and high-Fe soils (Lucey et al., 2000a). The FeO maps derived from these two regions are shown in Fig. 4, and the corresponding statistical results are shown in Fig. 5.

In Fig. 4, it can be observed that most of the fresh craters exhibited to be bright in the reflectance images are invisible from all the PLS-derived FeO maps, which indicates that the maturity has been well suppressed by the PLS models. The homogeneity (can be measured by standard deviation) of FeO-1 iron map is worse than the maps of other two FeO models, which might be induced by the noise of IIM images or a worse maturity suppressing ability. The FeO maps of Model-2 and Model-3 are very similar to the result of Ling et al. (2013), whose model is based on band-ratio method following Lucey et al. (2000a), indicating that the maturity suppressing ability of Model-2 and Model-3 are as good as band ratio algorithm.

The histograms of FeO content in Fig. 5a have a bimodal distribution, the left peak (peak1) represents the abundance of FeO in highland region and the right peak (peak2) presents that in mare region. The lower iron values in the highlands are due to abundant plagioclase, while mare regions are filled with Fe-rich mafic basalts. We resample the same region of Clementine UVVIS images (at 100 m/pixel) to IIM resolutions (at 200 m/pixel) by 2 × 2 pixels average, making it convenient for comparing our result with Lucey et al. (2000a) result. The FeO contents for peak1 of the three PLS models are almost the same (9–10 wt%), and this value is about 1.5 wt% higher than that derived by Ling et al. (2013). As for the FeO content of peak2, the result of PLS Models are around 16 wt%, which is 0.1–0.3 wt% higher than the result of Ling et al. (2013). The FeO content of peak1 and peak2 from Clementine iron map are 9.0 and 16.9 wt%, and peak2 value is ~0.9 wt% higher than IIM. The effect of TiO_2 content in FeO mapping is examined by PLS modeling with the mare region of west Oceanus Procellarum (Fig. 4b), where is low-Ti and high-Fe basalts. The average abundance of TiO_2 for this region is ~2.8 wt% as calculated by the equations from Ling et al. (2013). As shown by Fig. 5b, the peak value of FeO concentrations derived by FeO-1 (14.9 wt%) and FeO-2 (14.6 wt%) are higher than the results of Ling et al. (2013) (14.4 wt%). Gillis et al. (2004) find that after adjusting the effect of TiO_2, a higher FeO content can be derived from the FeO algorithm for high-Fe, low-Ti soils. However, although Model-3 directly add TiO_2 content as a parameter while modeling, it has the lowest FeO content (14.2 wt%), implying the TiO_2 compositional effects is worse constrained in comparison with the other two models. FeO-2 is both sensitive to the compositional effect of TiO_2 and performs well in maturity suppressing, thus is our favored PLS-derived FeO model in this study.

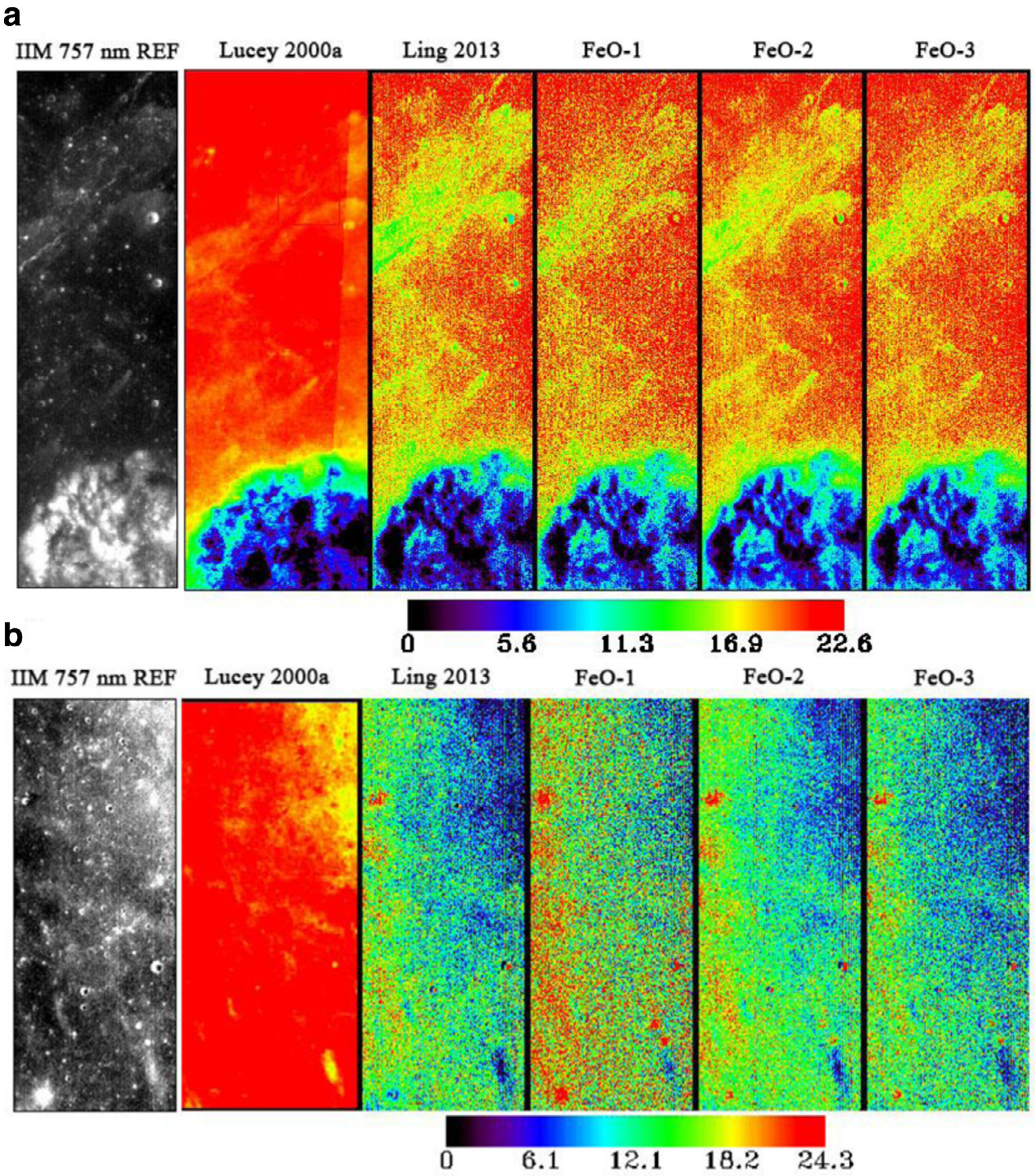

Fig. 4. Reflectance at 757 nm from IIM, and FeO maps derived from Lucey et al. (2000a), Ling et al. (2013) and from the three FeO models presented herein. (a) The south of Mare Crisium, and this region contains both mare and highland area (center coordinate: 61°E, 11°N). (b) East Oceanus Procellarum (center coordinate: 39.5°W, 15°N), the soil of which is suggested to be low-Ti and high-Fe based on the Clementine global FeO and TiO_2 maps derived by the equations from Lucey et al. (2000a) and IIM map by the equations from Ling et al. (2013).

5. Global mapping of FeO and OMAT

5.1. Global distributions of FeO

We derive the global distribution of FeO by applying FeO-2 to the global mosaic of IIM dataset (Fig. 6a). The nearside mare basins show abundant FeO, while the farside is short of FeO. This result is to be expected due to the fact that the mare basalts consist of FeO-rich mafic minerals and highland rocks are mainly FeO-poor feldspathic minerals (Taylor et al., 2006). In order to further correct potential systematic errors of our global FeO quantification we compare the PLS-derived global FeO map with that derived from LP gamma ray spectrometer (GRS) data (Prettyman et al., 2006). LP-GRS FeO map is more reliable through direct measures (the counting rate of 7.6 MeV gamma ray lines) of iron abundances immune to possible space weathering effects (Lawrence et al., 2002), although it has coaser spatial resolution (>15 km/pixel) than that of IIM (~200 m/pixel). By resampling the IIM and LP maps into the same spatial resolution (0.5°/pixel, Fig. 6b), it is evident that most of the differences of the FeO distributions between the result of PLS and LP are within ±3.0 wt%, while LP derived a much higher FeO content in middle Mare Imbrium and Oceanus Procellarum. PLS-derived FeO map seems to have higher FeO values in high latitude areas, which might be the result of topographic shading (caused by large phase angle) and/or residual effect of photometric correction in these regions (Lucey et al., 1998a). PLS-derived

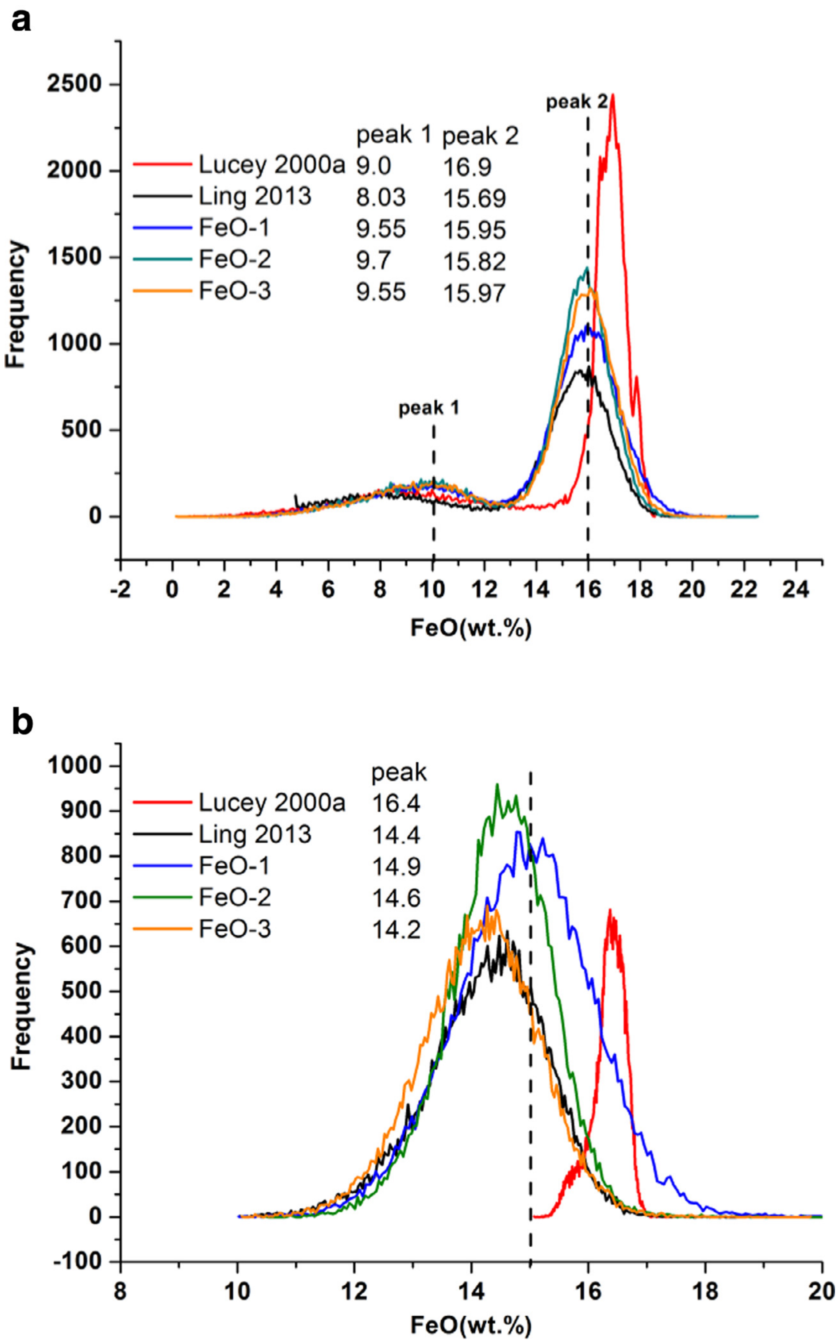

Fig. 5. Histograms corresponding to the FeO maps shown in Fig. 4, and derived from different models.

FeO map shows an overestimation in high latitude regions and an underestimation in mare regions, suggesting further calibration is needed for the quantification of FeO contents.

We resample IIM FeO map and LP-GRS FeO map (Prettyman et al., 2006) to the same 0.5° resolution, and scatter plot LP versus PLS result in Fig. 7a, the correlation between them is quadratic rather than linear (Lawrence et al., 2002). The PLS-derived FeO values are corrected by LP-GRS result with a quadratic fitting (Eq. 11). After the correction, a linear relationship can be achieved between IIM and LP FeO maps (Fig. 7b).

$$\mathrm{LP} = (0.0731\mathrm{PLS}^2) + (-0.3934\mathrm{PLS}) + 4.0885 \qquad (11)$$

The corrected IIM FeO map (PLS corrected) is shown in Fig. 6c. The former global mode of the PLS-derived FeO content is ~7.2 wt% and the cut off value is ~20 wt% (Fig. 8). After the correction, the FeO map is improved by a decrease in highland FeO content and an increase in mare FeO content (Fig. 6). The global mode (4.8 wt%) and mean value (7.4 wt%) of this FeO map is more consistent with the result of Prettyman et al. (2006) (mode = 4.7 wt%, mean = 7.3 wt%) (Fig. 8). The global mode of the FeO map from Clementine spectral reflectance (CSR) is ~5.8 wt% after being linearized by LP-GRS data (Lawrence et al., 2002), and it is about 1.0 wt% higher than our result. Korotev et al. (2003) obtained an average FeO content of 4.4 ± 0.6 wt% from a systematic study of 11 feldspathic meteorites, indicating the FeO concentrations of typical anorthositic lunar highlands are less than 5.0 wt%. The global mode of a FeO map is representative of the peak FeO concentrations in lunar highland regions. The mode of the corrected PLS (4.8 wt%) FeO

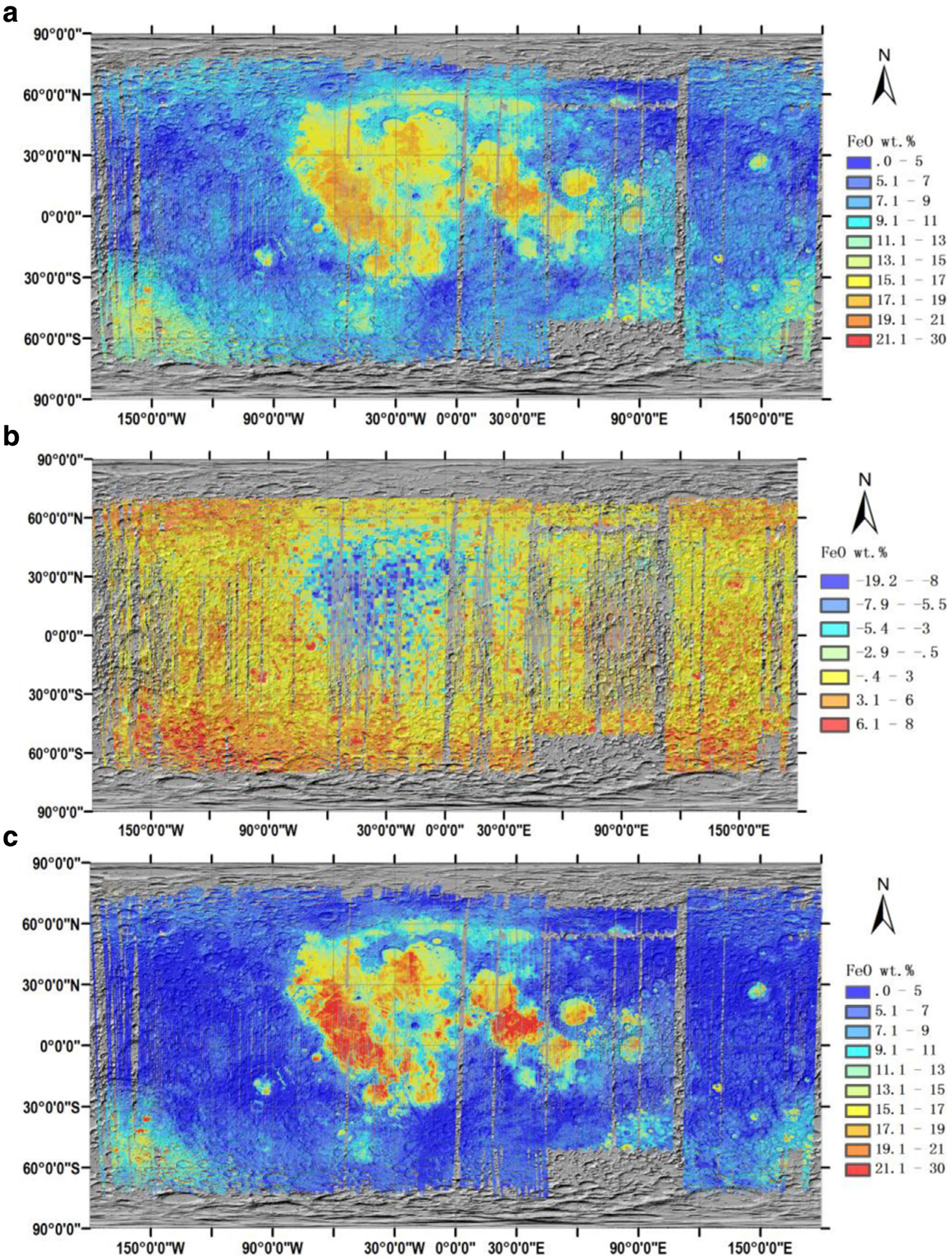

Fig. 6. Global maps derived from IIM mosaic, all of the maps are at 800 m resolution except that the image in (b) has been resampled to 0.5° /pixel, and background is Kaguya topography. (a) The FeO map derived from PLS Model-2 (Eq. 9). (b) The difference between the FeO map using the PLS FeO-2 model and the LP-GRS map from Prettyman et al. (2006). (c) is the FeO map of the corrected PLS Model.

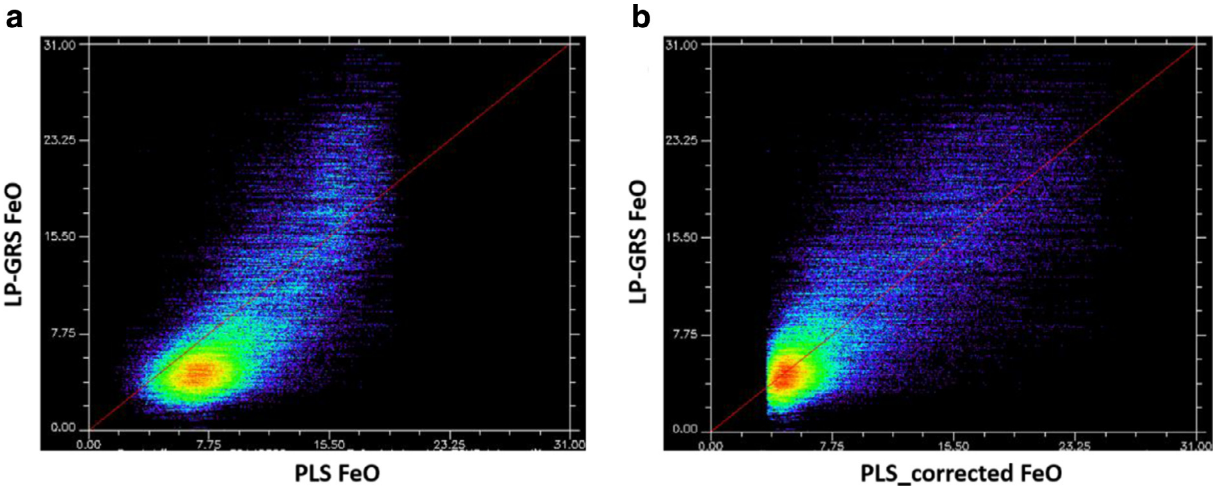

Fig. 7. The 2D scatter plots of global FeO maps derived by PLS versus FeO from LP-GRS derived by Prettyman et al. (2006), (a) LP versus PLS results, (b) LP versus corrected PLS results. All the maps have been resampled to 0.5° /pixel and the red line is the 1:1 line.

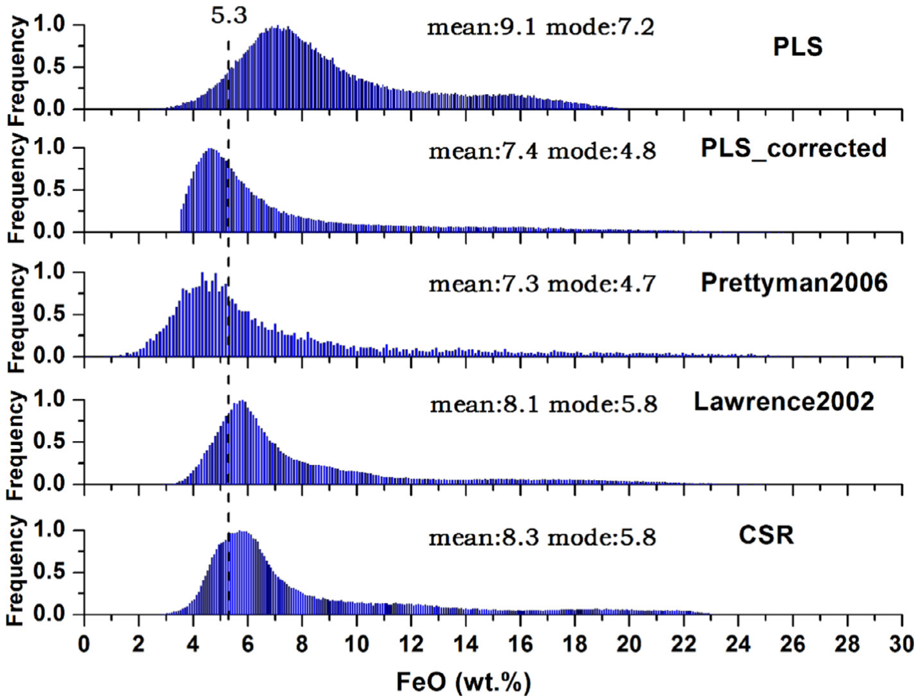

Fig. 8. Histograms of the global distribution of FeO content, with the frequency being normalized to 1.0. From the top to bottom are: the result of PLS model FeO-2 and PLS model FeO-2 result corrected by the FeO map of LP-GRS, LP-GRS result at 2° resolution derived by Prettyman et al. (2006), LP-GRS result of Lawrence et al. (2002) and the linearized result of Clementine spectral reflectance (CSR) (Lawrence et al., 2002). For the convenience of comparison between these works, all the maps used to derive histograms have been resampled to 0.5° resolution. The average FeO content of Apollo 16 sampling sites (5.3 wt.%) is marked with a dashed line.

map and Prettyman-2006 (4.7 wt%) FeO map are more consistent with lunar feldspathic meteorites study than the others mentioned above (>5.0 wt%). According to the geochemical studies of lunar feldspathic meteorites (which are assumed as randomly sampling the lunar highlands) and their incompatible elements, the Apollo 16 highland samples have been suggested not to be typical highland soils (Gross et al. 2014; Korotev et al., 2003; Warren, 1990). The FeO contents of representative Apollo 16 lunar samples (Lucey et al., 2000a) are ~5.3 wt% on average (indicated by the dashed line in Fig. 8). The global mode of the corrected PLS FeO map is 4.8 wt%, suggesting that most of the highland materials are poorer in Fe (more anorthositic) than Apollo 16 lunar samples. Thus our FeO mapping of highland regions supports that Apollo 16 soils may not be typical highland soils. We also examined the FeO abundance at the Chang'E-3 (CE-3) landing site using the corrected PLS FeO map, and the value is ~20.7 wt%, in accordance with 22.8 ± 2.1 wt% measured by the active particle-induced X-ray spectrometer (APXS) onboard Yutu rover (Ling et al., 2015). Therefore, the corrected PLS FeO map is in agreement with the both the low-FeO (feldspathic meteorites) and high-FeO (CE-3 site) endmembers, and moreover, it combines the advantages of high resolution of IIM images and the accurate FeO content of LP-GRS.

The global distribution of FeO contents can be used as the discriminators for different types of lunar surface materials (e.g., minerals assemblages, soils, and rock types). We classify the abundance of FeO into 6 groups (3 for highlands and 3 for mare regions) with corrected PLS FeO map (Fig. 9a), with intent to better understand the iron distribution of different lunar terrains.

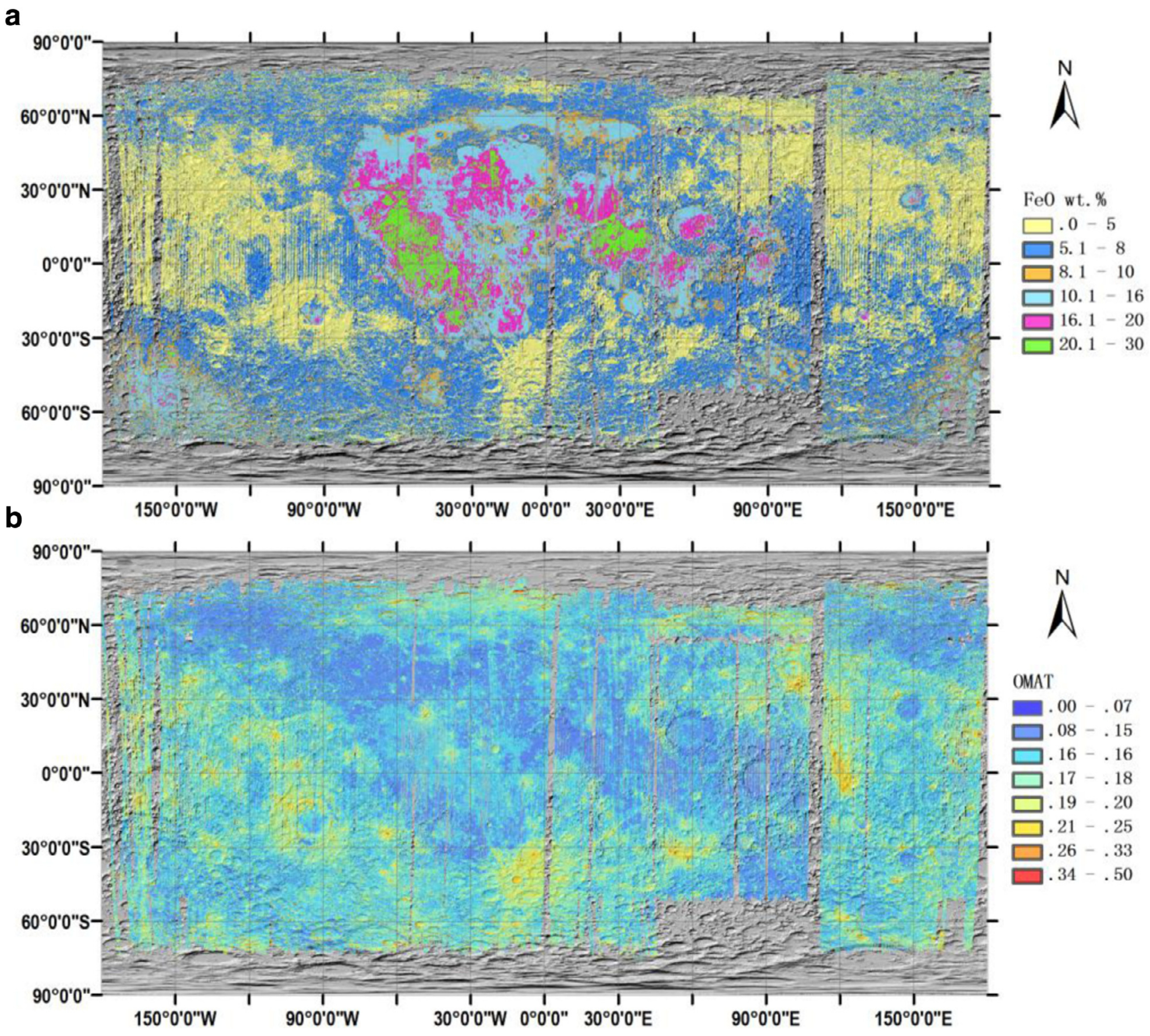

Fig. 9. (a) Lunar global FeO map derived from the corrected PLS model FeO-2 (same to Fig. 6c, but with different classification of iron values), (b) global OMAT map derived from the OMAT model (Eq. (7)).

According to the lunar sample analysis (Haskin and Warren, 1991), the boundary of highlands and mare can be determined as 8–10 wt% FeO, i.e., $<$8 wt% FeO regions are classified as highlands, $>$10 wt% FeO regions are classified as mare. Highland regions show an inhomogeneous FeO distribution (Fig. 9) and can be further divided into two parts: the feldspathic highland region (0–5 wt%) and the mixed highland region (5–8 wt%). Except for the feldspathic materials located near Orientale and Tycho, the feldspathic highland region is mostly concentrated in the northern farside of the Moon, which is consistent with the Feldspathic Highlands Terrain (FHT) proposed by Jolliff et al. (2000). The mixed highland regions are evident (in Fig. 9a) on the boundaries between those feldspathic highlands and mare regions, which is probably caused by the contamination from the high-FeO basaltic ejecta of the nearside mare. Mare regions are classified to three kinds of FeO concentrations: ultrahigh ($>$20 wt%), high (16–20 wt%) and medium (10–16 wt%). Different geological basaltic units can be distinguished via the variation of FeO abundances. Regions from northern Oceanus Procellarum, northeast Mare Imbrium and Sinus Iridum have medium FeO concentrations and are regarded as older Imbrian basalts (Hiesinger et al., 2000; Thiessen et al., 2014). Whereas the western Oceanus Procellarum and central Mare Imbrium have high to ultrahigh FeO concentrations and are considered to be younger Eratosthenian lava flows (Hiesinger et al., 2003; Thiessen et al., 2014). We also compare the FeO abundance of corrected PLS model with LP-GRS FeO map (Prettyman et al., 2006) and the linearized CSR FeO map (Lawrence et al., 2002) for SPA region after resampling these three maps to the same 0.5° resolution. SPA region is suggested to contain LKFM (Low-K Fra Mauro) basalt, which has ~8.8 wt% FeO on average (Lawrence et al., 2002; Lucey et al., 1998b; Vaughan and Head, 2014). The peak concentration of FeO for SPA region derived by corrected PLS model is ~9.0 wt%, with some exposures exceeding 10 wt% (Fig. 10). Our result is consistent with the hypothesis that SPA consists of LKFM rocks with some enrichment of FeO-rich upper mantle materials (Jolliff et al., 2000; Lawrence et al., 2002; Lucey et al., 1998b).

5.2. The relation of OMAT and age for young mare basaltic units

A maturity parameter is intended to reflect the long-term accumulation of space weathering products, such as SMFe and ag-

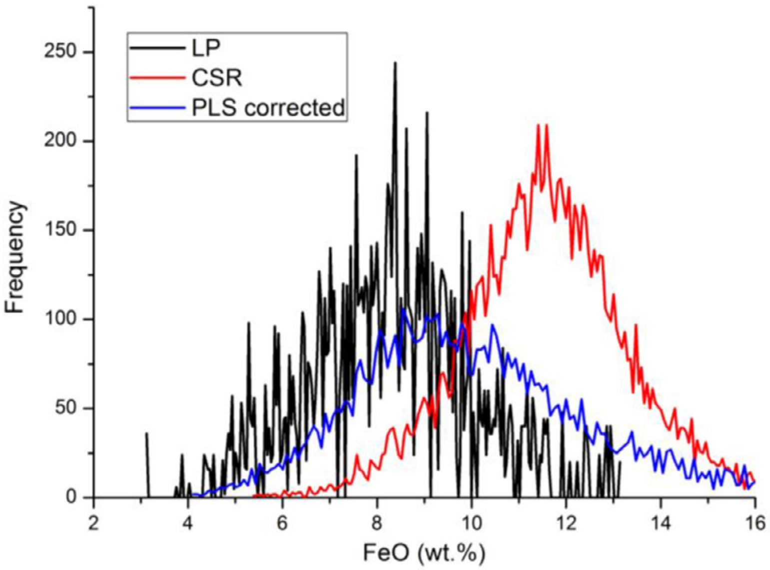

Fig. 10. Histograms of the FeO abundances for SPA region. The LP FeO map (Prettyman et al., 2006), linearized CSR FeO map (Lawrence et al., 2002; Lucey et al., 2000) and corrected PLS FeO map of IIM (this work) has been resampled to 0.5° before comparison.

glutinates (Fischer and Pieters, 1994). The OMAT value is one of the maturity indices widely used for lunar spectral remote sensing studies (e.g., Lucey et al., 2000b; Nettles et al., 2011). In principle, OMAT values should relate to the ages of certain lunar rock units, which are determined by the duration time of space weathering that lunar materials have undergone. Fresher materials have been experienced a shorter time of space weathering, thus have high OMAT values; older materials have experienced a longer time of space weathering, thus have low OMAT values, and their maturity might have already saturated (Lucey et al., 2000b). However, different compositional and mineralogical features of lunar rock units also affect their VIS-NIR spectral features, thus lead to complex effects need in-depth analysis. In fact, the Moon is a very nice "laboratory" for our understanding of billions of years space weathering effects on its surface units, especially those young lunar basaltic units whose OMAT may not saturated.

The global OMAT map derived from Eq. (7) is shown in Fig. 9b. This map shows the lunar highland and mare regions have no obvious dichotomy, indicating the compositional differences between those two terrains have been well suppressed in our OMAT mapping . Young lunar craters (e.g., Tycho and Aristarchus) usually have OMAT values higher than 0.25 (Lucey et al., 2014) with bright ejecta rays in our OMAT map, thus this OMAT map can be used as a tool to distinguish young impact events.

It has been shown that OMAT would be saturated for mature (Is/FeO $\geq$ 50) lunar soils (Lucey et al., 2000b). Young lunar mare basalts have undergone less space weathering and their OMAT may have not reached saturation. Therefore, we can correlate their OMAT values with ages, in order to estimate the space weathering effects on lunar basalts with different ages. Here we make a statistics of the OMAT values of 41 youngest (<3.0 Ga) lunar mare units (Morota et al., 2011) (including 29 units from Oceanus Procellarum, 10 units from Mare Imbrium and 2 units from Mare Insularum). During the calculation of the average OMAT value for each basaltic unit, the individual statistical area for OMAT is carefully selected within the crater size-frequency counting areas used by Morota et al. (2011). We exclude those obvious visible large and/or fresh craters and their ejecta in case of their influences of the “true” OMAT values of the local mare basalts. The OMAT values, FeO and TiO_2 contents of 41 geological units are listed in Table 3, and their OMAT values versus ages are plotted in Fig. 11. The FeO content is calculated with Eq. (9) and the TiO_2 content is calculated with equations from Ling et al. (2013). For the convenience of comparisons, we divide these units into three groups based on their FeO and TiO_2 contents: ultrahigh-Fe & Ti (FeO $>$ 20 wt% and TiO_2 $>$10 wt%), high-Fe & Ti (FeO $\approx$ 16–20 wt% and TiO_2 $\approx$ 8.5–10 wt%) and medium-Fe & Ti (FeO $<$ 16 wt% and TiO_2 $<$ 8.5 wt%) (Giguere et al., 2000; Ling et al., 2014a).

An overall inverse correlation (Fig. 11) shows older lunar basalts tend to have lower OMAT values. This is to be expected that older lunar mare surface has undergone longer exposure time and thus accumulated more space weathering products including SMFe and agglutinates. For units with ultrahigh-Fe & Ti, OMAT shows a weak correlation with age (R^2 $<$ 0.01, Fig. 11). Whereas the OMAT shows a relatively good linearity with age for units has medium to high-Fe & Ti ($R^2 \approx 0.45$, Fig. 11). Hence, OMAT is correlated with age for lunar young basalts with medium to high-Fe & Ti.

OMAT of ultrahigh-Fe & Ti units are weakly correlated with ages, which may be the result of:

(1) The spectroscopic influence of abundant ilmenite. Ultrahigh TiO_2 content of the lunar soils suggest the existence of abundant ilmenite, which would lead to blue shift and flatter of the VIS-NIR spectra (Hapke et al., 1975; Lucey et al., 1998a). While the maturity effects of lunar soils will induce a red shift of the observed remotely sensed spectra (Hapke et al., 1975; Lucey et al., 1998a). Therefore, the presence of ilmenite would reduce the spectral reddening effect of lunar soils, which thus appear to be fresher (i.e., higher OMAT value) materials. On the other hand, the existence of opaque mineral (i.e., ilmenite, Isaacson et al., 2011) would also make the soils appear to be darker and more mature. These two phenomena compete with each other yet coexist in ilmenite-rich basaltic soils. Ultrahigh-Fe & Ti units tend to be fresher than other groups based on our observations of young basaltic units (<3Ga), suggesting the bluish effect of the ilmenite may dominate the reflectance variations.

(2) The unique space weathering mechanism of ultrahigh-Fe & Ti soils. That means ilmenite may have gone through a different weathering processes from other minerals. Fu et al. (2012) simulated the space weathering process of ilmenite using terrestrial samples, and they measured the reflectance spectral variations from 375 to 2500 nm. After being irradi-

Table 3
The OMAT, age and chemical contents of 41 geological units.

Unit[a]	Age (Ga)[a]	Omat[b]	FeO (wt%)[b]	TiO_2 (wt%)[b]	Unit[a]	Age (Ga)[a]	Omat[b]	FeO (wt%)[b]	TiO_2 (wt%)[b]
P60	1.73	0.160	19.3	9.7	P36	2.48	0.138	12.8	7.0
P59	1.81	0.144	16.4	8.6	P35	1.5	0.153	24	11.2
P58	1.91	0.143	16.9	8.8	P34	2.87	0.147	22	10.6
P57	1.73	0.152	22.5	10.8	P32	1.79	0.151	20.6	10.1
P56	2.34	0.135	16.9	8.9	P28	2.87	0.135	12.7	6.9
P55	2.5	0.138	17.9	9.3	P27	2.73	0.151	21	10.3
P54	2.06	0.144	19.8	9.9	P25	2.05	0.145	17	8.8
P53	2.1	0.144	20.2	10.0	P24	2.6	0.152	20.4	10.1
P52	1.87	0.151	20.8	10.2	IN4	2.31	0.155	14.1	7.4
P51	1.84	0.154	19.8	9.8	IN3	2.1	0.149	17.4	8.9
P50	2.2	0.158	16.9	8.7	I30	1.96	0.151	16.6	8.7
P49	1.71	0.150	24	11.2	I29	1.86	0.147	18.6	9.5
P48	1.85	0.153	14.6	7.8	I28	2.01	0.144	19.3	9.7
P47	2.19	0.149	20.9	10.3	I27	2.44	0.127	14.4	7.8
P46	1.76	0.150	17.4	8.9	I26	1.98	0.142	18	9.3
P45	1.88	0.155	22.5	10.7	I25	2.55	0.139	14.2	7.7
P44	2.15	0.148	23.5	11.2	I24	2.48	0.125	15.4	8.3
P43	1.58	0.147	21.6	10.5	I23	2.68	0.135	15.6	8.3
P40	2.56	0.132	14.6	7.9	I22	1.98	0.138	20	10.1
P39	1.97	0.137	17.5	9.1	I4	2.04	0.148	19.1	9.6
P38	1.91	0.146	18.8	9.5					

[a] The counting area of each unit is according to the work of Morota et al. (2011), and fresh craters as well as ejecta of fresh craters are excluded to avoid contamination from fresh materials.

[b] OMAT is calculated with Eq. (7), FeO content is derived from the corrected PLS model (FeO-8) and TiO_2 content is calculated using equations of Ling et al. (2013) using IIM spectral images.

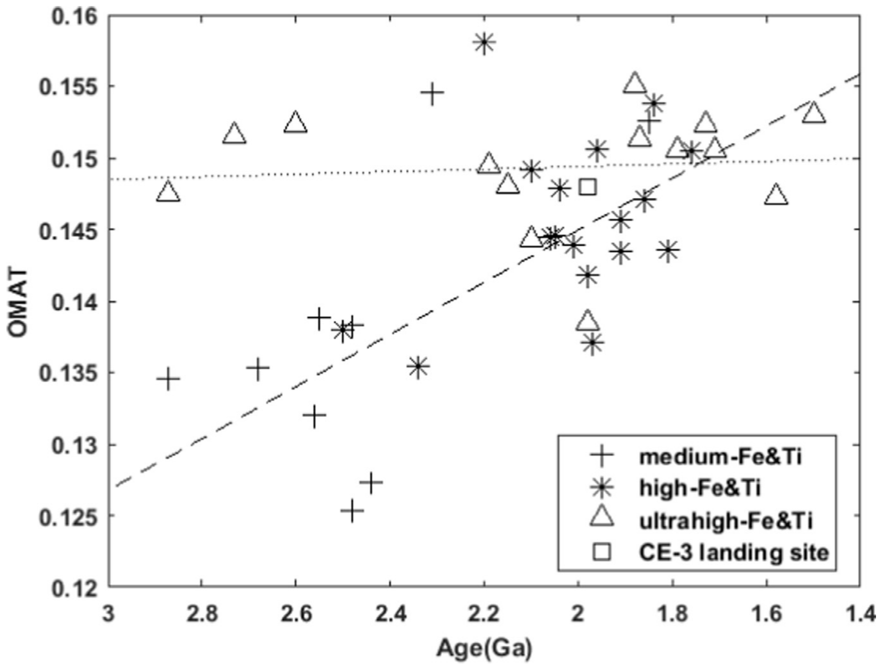

Fig. 11. OMAT versus Age of geological units from lunar nearside mare for medium, high and ultrahigh Fe & Ti. Medium Fe & Ti units (pluses) correspond to geological units with <16 wt% FeO and <8.5 wt% TiO_2, high-Fe & Ti units (asterisks) correspond to geological units that have 16–20 wt% FeO and 8.5–10 wt% TiO_2, ultrahigh-Fe & Ti units (triangles) correspond to geological units that have >20 wt% FeO and > 10 wt% TiO_2. The dashed line is a regression line fit medium to high-Fe & Ti units and the correlation coefficient is ~0.45. The dotted line represents a regression fit to units with ultrahigh-Fe, Ti and the correlation coefficient is below 0.01. The OMAT value and age of the landing site of Chang'E-3 (20.66 wt% FeO, 10.23 wt% TiO_2) has been marked with a square on the plot.

ated with 50 keV He^+, higher reflectance and stronger absorption features are observed from ilmenite spectra, suggesting the ilmenite has become fresher (Fu et al., 2012). When the abundance of ilmenite reaches a high level (e.g., 10 wt%), the reflectance of the lunar soils may be significantly affected and presented to be fresher.

The different trend of ultrahigh-Fe & Ti basalts is caused by abundant ilmenite, but the detailed space weathering process of ilmenite are complicated and need more experimental work to validate.

6. Conclusions

New OMAT and FeO models of Chang'E-1 IIM data are built with Partial Least Squares regression considering the influence of TiO_2 abundances and space weathering effect. Global FeO corrected with LP-GRS FeO map shows a quantitatively reasonable result, which is consistent with previous remote sensing results (Ling et al., 2016; Ling et al., 2011b; Prettyman et al., 2006) as well as lunar feldspathic meteorite studies (Korotev et al., 2003) and the Chang'E-3 landing site (Ling et al., 2015). Although the wavelength range of IIM spectra are limited, a valid FeO model was still achieved with PLS regression and physical parameters, indicating this method is promising for other imaging spectral datasets similar to IIM (e.g. Visible and InfraRed (VIR) on DAWN and Mercury Dual Imaging System (MDIS) on MESSENGER). Based on the new FeO map by Chang'E-1, we discover an obvious compositional inhomogeneity across lunar highland regions, which have not been suggested by previous datasets (e.g., Clementine UVVIS). Furthermore, we suggest that at least part of the FeO enrichments would be caused by mixing of highland and mare, as the FeO enrichment are seen around the major mare regions. The new PLS derived OMAT map is effective in suppressing the compositional differences between highlands and mare regions. We examined the correlation between OMAT and age for basalts younger than 3 Ga and find that OMAT values show a linear decrease with ages, suggesting the OMAT value is well correlated with the age of young lunar basalts with medium to high FeO (< 20 wt% FeO) and TiO_2 (<10 wt% TiO_2) contents. Basaltic units with ultrahigh FeO and TiO_2, OMAT values tend to be higher and varies little with ages, which may be the result of the unique optical maturity effects of abundant ilmenite.

Acknowledgements

The Clementine data is from U.S. Geological Survey (USGS) and the LROC images are from NASA/GSFC/Arizona State University. This research was supported by the National Natural Science Foundation of China (41473065, 41373068, U1231103, 41490634), National Science and Technology Infrastructure Work Projects (2015FY210500), the Natural Science Foundation of Shandong Province (JQ201511 and ZR2015DQ001), Qilu (Zhongying) Young Scholar of Shandong University and Young Scholars Program of Shandong University, Weihai (2015WHWLJH14).

Supplementary materials

Supplementary material associated with this article can be found, in the online version, at doi:10.1016/j.icarus.2016.07.010.

References

Adams, J.B., Goullaud, L.H., 1978. Plagioclase feldspars: Visible and near infrared diffuse reflectance spectra as applied to remote sensing. In: Lunar and Planetary Science IX, pp. 1–3.

Blewett, D.T., Lucey, P.G., Hawke, B.R., et al., 1997. Clementine images of the lunar sample-return stations: Refinement of FeO and TiO_2 mapping techniques. J. Geophys. Res.: Planets 102, 16319–16325.

Cousin, A., Meslin, P.Y., Wiens, R.C., et al., 2015. Compositions of coarse and fine particles in martian soils at gale: A window into the production of soils. Icarus 249, 22–42.

Cousin, A., Sautter, V., Fabre, C., et al., 2012. Textural and modal analyses of picritic basalts with ChemCam laser-induced breakdown spectroscopy. J. Geophys. Res.: Planets 117, E10002.

Dyar, M.D., Carmosino, M.L., Breves, E.A., et al., 2012. Comparison of partial least squares and lasso regression techniques as applied to laser-induced breakdown spectroscopy of geological samples. Spectrochim. Acta Part B: Atom. Spectrosc. 70, 51–67.

Fischer, E.M., Pieters, C.M., 1994. Remote Determination of exposure degree and iron concentration of lunar soils using VIS-NIR spectroscopic methods. Icarus 111, 475–488.

Fischer, E.M., Pieters, C.M., 1996. Composition and exposure age of the Apollo 16 Cayley and Descartes regions from clementine data: Normalizing the optical effects of space weathering. J. Geophys. Res.: Planets 101, 2225–2234.

Fu, X., Zou, Y., Zheng, Y., et al., 2012. Effects of space weathering on diagnostic spectral features: Results from He+ irradiation experiments. Icarus 219, 630–640.

Giguere, T.A., Taylor, G.J., Hawke, B.R., et al., 2000. The titanium contents of lunar mare basalts. Meteorit. Planet. Sci. 35, 193–200.

Gillis-Davis, J.J., Lucey, P.G., Hawke, B.R., 2006. Testing the relation between UV–vis color and TiO_2 content of the lunar maria. Geochim. Cosmochim. Acta 70, 6079–6102.

Gillis, J.J., Jolliff, B.L., Korotev, R.L., 2004. Lunar surface geochemistry: Global concentrations of Th, K, and FeO as derived from lunar prospector and Clementine data. Geochim. Cosmochim. Acta 68, 3791–3805.

Green, R.O., Pieters, C., Mouroulis, P., et al., 2011. The Moon mineralogy mapper (M3) imaging spectrometer for lunar science: Instrument description, calibration, on-orbit measurements, science data calibration and on-orbit validation. J. Geophys. Res.: Planets 116, E00G19.

Gross, J., Treiman, A.H., Mercer, C.N., 2014. Lunar feldspathic meteorites: Constraints on the geology of the lunar highlands, and the origin of the lunar crust. Earth Planet. Sci. Lett. 388, 318–328.

Hapke, B., 2001. Space weathering from Mercury to the asteroid belt. J. Geophys. Res.: Planets 106, 10039–10073.

Hapke, B., Danielson, G.E., Klaasen, K., et al., 1975. Photometric observations of Mercury from Mariner 10. J. Geophys. Res. 80, 2431–2443.

Haskin, L., Warren, P., 1991. Lunar Source Book: A User's Guide to the Moon. Cambridge University Press, London.

Hiesinger, H., Head, J.W., Wolf, U., et al., 2003. Ages and stratigraphy of mare basalts in Oceanus Procellarum, Mare Nubium, Mare Cognitum, and Mare Insularum. J. Geophys. Res.: Planets 108, 5065.

Hiesinger, H., Jaumann, R., Neukum, G., et al., 2000. Ages of mare basalts on the lunar nearside. J. Geophys. Res.: Planets 105, 29239–29275.

Isaacson, P.J., Sarbadhikari, A.B., Pieters, C.M., et al., 2011. The lunar rock and mineral characterization consortium: Deconstruction and integrated mineralogical, petrologic, and spectroscopic analyses of mare basalts. Meteorit. Planet. Sci. 46, 228–251.

Jolliff, B.L., Gillis, J.J., Haskin, L.A., et al., 2000. Major lunar crustal terranes: Surface expressions and crust-mantle origins. J. Geophys. Res.: Planets 105, 4197–4216.

Kooistra, L., Wehrens, R., Leuven, R.S.E.W., et al., 2001. Possibilities of visible–near-infrared spectroscopy for the assessment of soil contamination in river floodplains. Anal. Chim. Acta 446, 97–105.

Korotev, R.L., Jolliff, B.L., Zeigler, R.A., et al., 2003. Feldspathic lunar meteorites and their implications for compositional remote sensing of the lunar surface and the composition of the lunar crust. Geochim. Cosmochim. Acta 67, 4895–4923.

Lawrence, D.J., Feldman, W.C., Elphic, R.C., et al., 2002. Iron abundances on the lunar surface as measured by the Lunar Prospector gamma-ray and neutron spectrometers. J. Geophys. Res.: Planets 107, 5130.

Le Mouélic, S., Langevin, Y., Erard, S., et al., 2000. Discrimination between maturity and composition of lunar soils from integrated Clementine UV–visible/near-infrared data: Application to the Aristarchus Plateau. J. Geophys. Res.: Planets 105, 9445–9455.

Le Mouélic, S., Lucey, P.G., Langevin, Y., et al., 2002. Calculating iron contents of lunar highland materials surrounding Tycho crater from integrated Clementine UV–visible and near-infrared data. J. Geophys. Res.: Planets 107, 5074.

Lemelin, M., Lucey, P.G., Song, E., et al., 2015. Lunar central peak mineralogy and iron content using the Kaguya Multiband Imager: Reassessment of the compositional structure of the lunar crust. J. Geophys. Res. Planets 120, 869–887.

Li, L., 2006. Partial least squares modeling to quantify lunar soil composition with hyperspectral reflectance measurements. J. Geophys. Res.: Planets 111, E04002.

Li, L., 2008. Quantifying lunar soil composition with partial least squares modeling of reflectance. Adv. Space Res. 42, 267–274.

Ling, Z.C., Jolliff, B.L., Wang, A., et al., 2015. Correlated compositional and mineralogical investigations at the Chang'e-3 landing site. Nat Commun 6, 8880. doi:10.1038/ncomms9880.

Ling, Z.C., 2011. The data processing and science inversion of Chang'E-1 IIM data. National Astronomical Observatories, Chinese Academy of Sciences, pp. 1–10.

Ling, Z.C., Liu, J.Z., Zhang, J., et al., 2014a. The lunar rock types as determined by Chang'E-1IIM data: A case study of Mare Imbrium Mare Frigoris region (LQ-4). Earth Sci. Front. 21, 107–120.

Ling, Z.C., Zhang, J., Liu, J.Z., 2012. An empirical nonuniformity correction of Chang'E-1 IIM Data. In: 43rd Lunar and Planetary Science Conference. The Woodlands, Texas abstract # 2213.

Ling, Z.C., Zhang, J., Liu, J.Z., 2013. Lunar iron and titanium distributions for LQ-4 region. In: 44th Lunar and Planetary Science Conference. The Woodlands, Texas abstract # 2992.

Ling, Z.C., Zhang, J., Liu, J.Z., et al., 2016. Lunar global FeO and TiO_2 mapping based on the recalibrated Chang'E-1 IIM dataset. Acta Petrol. Sin. 32, 87–98.

Ling, Z.C., Zhang, J., Liu, J.Z., et al., 2011a. Preliminary results of FeO mapping using Imaging Interferometer data from Chang'E-1. Chin. Sci. Bull. 56, 376–379.

Ling, Z.C., Zhang, J., Liu, J.Z., et al., 2011b. Preliminary results of TiO_2 mapping using imaging interferometer data from Chang'E-1. Chin. Sci. Bull. 56, 2082–2087.

Ling, Z.C., Zhang, J., Wu, Z.C., et al., 2014b. The spectral calibration of Chang'e-1 IIM Dataset. In: 45th Lunar and Planetary Science Conference. The Woodlands, Texas abstract # 1831.

Lucey, P.G., Blewett, D.T., Hawke, B.R., 1998a. Mapping the FeO and TiO_2 content of the lunar surface with multispectral imagery. J. Geophys. Res.: Planets 103, 3679–3699.

Lucey, P.G., Blewett, D.T., Jolliff, B.L., 2000a. Lunar iron and titanium abundance algorithms based on final processing of Clementine ultraviolet-visible images. J. Geophys. Res.: Planets 105, 20297–20305.

Lucey, P.G., Blewett, D.T., Taylor, G.J., et al., 2000b. Imaging of lunar surface maturity. J. Geophys. Res.: Planets 105, 20377–20386.

Lucey, P.G., Norman, J.A., Crites, S.T., et al., 2014. A large spectral survey of small lunar craters: Implications for the composition of the lunar mantle. Am. Mineral. 99, 2251–2257.

Lucey, P.G., Taylor, G.J., Hawke, B.R., et al., 1998b. FeO and TiO_2 concentrations in the South Pole-Aitken basin: Implications for mantle composition and basin formation. J. Geophys. Res.: Planets 103, 3701–3708.

Lucey, P.G., Taylor, G.J., Malaret, E., 1995. Abundance and distribution of iron on the Moon. Science 268, 1150–1153.

McKay, D.S., Heiken, G., Basu, A., et al., 1991. The lunar regolith. Lunar sourcebook 285–356.

Morota, T., Haruyama, J., Ohtake, M., et al., 2011. Timing and characteristics of the latest mare eruption on the Moon. Earth Planet. Sci. Lett. 302, 255–266.

Nettles, J.W., Staid, M., Besse, S., et al., 2011. Optical maturity variation in lunar spectra as measured by Moon mineralogy mapper data. J. Geophys. Res.: Planets 116, E00G17.

Ohtake, M., Haruyama, J., Matsunaga, T., et al., 2008. Performance and scientific objectives of the SELENE (KAGUYA) Multiband Imager. Earth, Planets Space 60, 257–264.

Ohtake, M., Matsunaga, T., Haruyama, J., et al., 2009. The global distribution of pure anorthosite on the Moon. Nature 461, 236–240.

Pieters, C., Shkuratov, Y., Kaydash, V., et al., 2006. Lunar soil characterization consortium analyses: Pyroxene and maturity estimates derived from Clementine image data. Icarus 184, 83–101.

Pieters, C.M., Stankevich, D.G., Shkuratov, Y.G., et al., 2002. Statistical analysis of the links among lunar mare soil mineralogy, chemistry, and reflectance spectra. Icarus 155, 285–298.

Pieters, C.M., Taylor, L.A., Noble, S.K., et al., 2000. Space weathering on airless bodies: Resolving a mystery with lunar samples. Meteorit. Planet. Sci. 35, 1101–1107.

Prettyman, T.H., et al., 2006. Elemental composition of the lunar surface: Analysis of gamma ray spectroscopy data from Lunar Prospector. J. Geophys. Res.: Planets 111, E12007. http://onlinelibrary.wiley.com/doi/10.1029/2005JE002656/full.

Qiu, Y.H., Wen, D.S., Zhao, B.C., et al., 2009. Interference imaging spectrometer of Chang'e-1 Satellite. Acta Photon. Sin 38, 484–488.

Robinson, M., Brylow, S., Tschimmel, M., et al., 2010. Lunar reconnaissance orbiter camera (LROC) instrument overview. Space Sci. Rev. 150, 81–124.

Shkuratov, Y.G., Stankevich, D.G., Kaydash, V.G., et al., 2003. Composition of the lunar surface as will be seen from SMART-1: A simulation using Clementine data. J. Geophys. Res.: Planets 108, 5020.

Taylor, S.R., Pieters, C.M., MacPherson, G.J., 2006. Earth-Moon System, planetary science, and lessons learned. Rev. Mineral. Geochem. 60, 657–704.

Thiessen, F., Besse, S., Staid, M.I., et al., 2014. Mapping lunar mare basalt units in mare Imbrium as observed with the Moon Mineralogy Mapper (M^3). Planet. Space Sci. 104, Part B, 244–252.

Vaughan, W.M., Head, J.W., 2014. Impact melt differentiation in the South Pole-Aitken basin: Some observations and speculations. Planet. Space Sci. 91, 101–106.

Wang, C., Wu, Y.Z., Shi, R.H., et al., 2013. The improvement of cross-calibration of IIM data and band selection for FeO inversion. Sci. China Phys., Mech. Astron. 56, 2216–2225.

Warren, P.H., 1990. Lunar anorthosites and the magma-ocean plagioclase-flotation hypothesis; importance of FeO enrichment in the parent magma. Am. Mineral. 75, 46–58.

Wilcox, B.B., Lucey, P.G., Gillis, J.J., 2005. Mapping iron in the lunar mare: An improved approach. J. Geophys. Res.: Planets 110, E11001.

Wu, Y.Z., 2012. Major elements and Mg# of the Moon: Results from Chang'E-1 interference imaging spectrometer (IIM) data. Geochim. Cosmochim. Acta 93, 214–234.

Wu, Y.Z., et al., 2012. Global estimates of lunar iron and titanium contents from the Chang' E-1 IIM data. J. Geophys. Res.: Planets 117, E02001.

Yan, B.K., Xiong, S.Q., Wu, Y.Z., et al., 2012. Mapping Lunar global chemical composition from Chang'E-1 IIM data. Planet. Space Sci. 67, 119–129.

Yen, A.S., Murray, B.C., Rossman, G.R., 1998. Water content of the martian soil: Laboratory simulations of reflectance spectra. J. Geophys. Res.: Planets 103, 11125–11133.

Zhang, J., Ling, Z.C., Zhang, W.X., et al., 2013. Photometric modeling of the Moon using Lommel-Seeliger function and Chang'E-1 IIM data. Chin. Sci. Bull. 58, 4588–4592.

Zuo, W., Li, C.L., Zhang, Z.B., 2014. Scientific data and their release of Chang'E-1 and Chang'E-2. Chin. J. Geochem. 33, 24–44.